Diagnostic sea ice predictability in the pan-Arctic and US Arctic regional seas

Wei Cheng[1,2], Edward Blanchard-Wrigglesworth[3], Cecilia M. Bitz[3], Carol Ladd[2], and Phyllis J. Stabeno[2]

[1]University of Washington, Joint Institute for the Study of Atmosphere and Ocean, Seattle, Washington, USA.

[2]NOAA/Pacific Marine Environmental Laboratory, Seattle, Washington, USA.

[3]University of Washington, Department of Atmospheric Science, Seattle, Washington, USA.

Corresponding author: Wei Cheng (wei.cheng@noaa.gov)

Key Points:

- While qualitatively similar, quantitative differences exist in ice area lagged correlation in models with or without data assimilation
- Regional predictability is strongly dependent upon location and season
- Pan-Arctic ice area summer (winter) limb memory intensifies (weakens) as the climate warms, but there are across-region variations

Abstract

This study assesses sea ice predictability in the pan-Arctic and US Arctic regional (Bering, Chukchi, and Beaufort) seas with a purpose of understanding regional differences from the pan-Arctic perspective, and how predictability might change under changing climate. Lagged correlation is derived using existing output from the CESM Large Ensemble (CESM-LE), Pan-Arctic Ice Ocean Modeling and Assimilation System (PIOMAS), and NOAA Coupled Forecast System Reanalysis (CFSR) models. While qualitatively similar, quantitative differences exist in Arctic ice area lagged correlation in models with or without data assimilation. On regional scales, modeled ice area lagged correlations are strongly location- and season-dependent. A robust feature in the CESM-LE is that the pan-Arctic melt-to-freeze season ice area memory intensifies whereas the freeze-to-melt season memory weakens as climate warms, but there are across-region variations in the sea ice predictability changes with changing climate.

1 Introduction

The US Arctic regional seas (Figure 1) are seasonally covered by sea ice, but also there is large interannual variability in the ice extent, thickness, and timing of ice arrival and retreat. Sea ice has a profound impact on regional oceanography and marine ecosystems. For example, in the Eastern Bering Sea, winter sea ice controls the extent of the so-called “cold pool” (bottom water with temperature < 2°C), and the latter plays an important role in the distributions of several commercially important fish species [e.g., *Wyllie-Echeverria and Wooster*, 1998]. The effect of ice presence and subsequent melting on ocean stratification can persist well into summer [*Stabeno et al.*, 2012*; Brown and Arrigo*, 2013], affecting the timing and magnitude of local primary production and influencing higher trophic levels. Despite its importance, our knowledge of sea ice predictability in this region is limited. Most sea ice predictability studies focus on pan-Arctic properties [e.g., *Blanchard-Wrigglesworth et al.*, 2011*; Tietsche et al.*, 2014*; Wang et al.*, 2012]. *Day et al.* [2014] touched on sub-basin scale sea ice predictability and found longer duration of ice-extent prediction skill in seasonal ice zones than in the central basins. They hypothesize that the longer time scale of predictability in regional seas is caused by interactions of sea ice with low-frequency climate variability. How robust this result is and whether it applies to other ice properties remains to be seen. Additionally, Arctic summer ice cover has experienced rapid decline in recent decades [*Cavalieri and Parkinson*, 2012*; Comiso and Hall*, *2014*], and further ice loss is expected under climate forcing scenarios [e.g., *Massonnet et al.*, 2012]. An emerging research question therefore is: Will sea ice predictability characteristics change as the background climate state changes and what mechanisms contribute to such change? Few studies have assessed the dependence of sea ice predictability on the mean-state. *Holland et al.* [2011] found that predictability of summer sea ice is lower in the 2010s compared to 1970s in the Community Climate System Model version 3 (CCSM3) simulations, and ascribed this change in predictability to transition to a thinner ice mean state in the model.

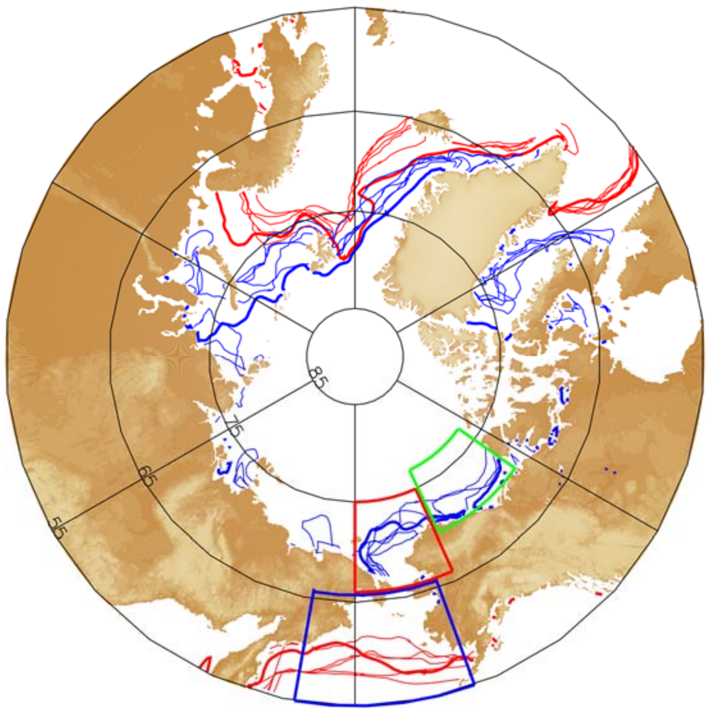

Figure 1. Study areas. The U.S. Arctic regional seas are composed of the blue, red, and green boxes denoting the Bering, Chukchi, and Beaufort seas, respectively. The pan-Arctic domain in this study is defined as north of 55°N. The thick red (blue) contours denote the 1979-2014 climatological mean 15% ice cover in March (September) from satellite sea ice concentration (SIC) using the NASA team algorithm. The thin red (blue) lines are March (September) 15% ice cover contours from one CESM-LE member in several years, demonstrating SIC interannual variability in this region.

Different metrics have been used to assess sea ice predictability. These include lagged correlation and root mean square error (RMSE). Lagged correlation measures inherent persistence of a variable or its diagnostic predictability. In comparison, RMSE requires ensemble integrations and quantifies the ensemble spread, which can be compared to the natural variability of a control climate, and is called a prognostic predictability metric. In this study, we examine lagged correlation of sea ice area and thickness in the US Arctic regional seas, in addition to the pan-Arctic mean states. Sea ice in these regions is influenced by advection and local formation and melting; these processes in turn are governed by surface forcing and regional oceanography [e.g., *Cheng et al.*, 2014]. The Bering Sea is composed of a wide, shallow eastern shelf and a deep ocean basin to the west. The southern Bering Sea shelf is covered by ice 3–4 months of the year and the northern Bering Sea shelf is ice covered 8–9 months of the year. The mean current direction in the eastern Bering Sea is northward, with a transport of 0.8 Sv (1 Sv = 10^6 m^3 s^{-1}) through the Bering Strait into the Chukchi Sea [*Woodgate et al.*, 2005]. The wind direction shifts seasonally over the Bering Sea, and is predominantly southwestward during winter and northward in the summer. The Chukchi Sea is composed primarily of a broad shelf with branches of northward flow influenced by ocean bottom topography, while a deep ocean basin is the predominant feature of the Beaufort Sea, whose circulation is dominated by the anticyclonic Beaufort gyre. The Beaufort Sea experiences extensive (> 90%) ice cover every year from November to approximately June, while the Chukchi Sea is 85% ice covered over the same period. Because of their different geographic layout and background ocean circulation, we consider these regions separately.

2 Methods

We use output from three comprehensive models: the Community Earth System Model Large Ensemble (CESM-LE), NCEP Climate Forecast System Reanalysis (CFSR), and University of Washington Pan-Arctic Ice Ocean Modeling and Assimilation System (PIOMAS). CESM-LE is a set of free-running simulations, while both CFSR and PIOMAS assimilate satellite sea ice concentration (SIC) data. We begin by comparing lagged correlation of pan-Arctic ice area and thickness and SST anomalies across outputs of these models and with satellite data to identify potential model biases. We then focus on the regional aspects of ice predictability in the CESM-LE. We conclude with an examination of how ice predictability may change under a changing background climate.

CESM is a global earth system model with interactive atmosphere, ocean, sea ice, and land processes. The CESM-LE is described in detail by *Kay et al.* [2015]. Briefly, we used a 30-member ensemble of CESM. The integrations were initialized from year 1920 and run to year 2100. The ensemble spread is generated by applying round-off perturbations to the initial atmospheric states, and so a few years after 1920, the members can be considered to be independent. Greenhouse gases and aerosol forcing are historical from 1920 to 2005 and follow the Representative Concentration Pathway 8.5 forcing thereafter. The CESM ocean and sea ice model spatial resolution is nominally 1° longitude by latitude; in the US Arctic regional seas, the mean spatial resolution is approximately 60 km.

CFSR is the latest reanalysis product created using the NCEP operational global Coupled seasonal Forecast System (CFS) for the period of 1979–2009. The CFS ocean component is based on the Geophysical Fluid Dynamics Laboratory (GFDL) Modular Ocean Model version 4 and the sea ice model is based on the GFDL Sea Ice Simulator. The mean horizontal resolution of ocean and sea ice models of CFS is 0.5° longitude by latitude. The main difference between CFSR and its predecessors is that CFSR uses a coupled framework. Hence, SST and sea ice are no longer prescribed lower boundary conditions in CFSR; instead, they are coupled to an interactive ocean and sea ice model. A suite of in situ and satellite products for the atmosphere, ocean and sea ice are assimilated in CFSR [*Saha et al.*, 2010].

PIOMAS, developed at the University of Washington Polar Science Center [*Zhang and Rothrock*, 2003], provides monthly mean sea ice variables from 1979 to near present (the latest month available from PIOMAS server is December, 2014). PIOMAS assimilates satellite-based ice concentration to improve ice thickness estimates; in addition, daily high-resolution Reynolds SST products [*Reynolds et al*., 2007] are assimilated in the ice-free areas. Atmospheric forcing from the NCEP/NCAR reanalysis is used to drive the PIOMAS model. For open lateral boundary located at 45°N, input from the Global Ice-Ocean Modeling and Assimilation System [*Lindsay and Zhang*, 2006] was used. The mean horizontal resolution of PIOMAS used in this study is 0.3° latitude by 0.8° longitude. PIOMAS has been extensively validated through comparisons with observations [*Schweiger et al.*, 2011].

In addition to the above model products, we also used monthly satellite passive microwave SIC data [*Meier et al.*, 2013; *Peng et al.*, 2013] from years 1979-2014, and monthly NOAA Optimum Interpolation (OI) Sea Surface Temperature V2 (provided by the

NOAA/OAR/ESRL at their web site http://www.esrl.noaa.gov/psd/) from years 1982-2014 in our analysis.

To obtain ice area, ice thickness, and SST anomalies in CESM-LE, we subtract the ensemble mean of each month from each ensemble member's monthly time series. This also effectively removes the long-term trend and mean seasonal cycle. For PIOMAS, CFSR, and satellite data, we remove the mean seasonal cycle and monthly linear trend at each grid point to obtain monthly anomalies. Corresponding anomalies at each grid box (including ice-free grid points) are averaged over the pan-Arctic domain (north of 55°N), the Bering (55–66°N, 170°E–160°W), Chukchi (66–75°N, 180°E–155°W), and Beaufort (70–77°N, 155–125°W) seas (Figure 1), respectively, to get domain mean anomalies. Ice area is calculated as a product of ice concentration (percentage) of each grid box and the grid box size, then summed over the respective domains to obtain regional ice area anomalies. Finally, monthly and domain-specific anomalies are used to compute correlation, with lags up to 15 months.

3 Results

3.1 Pan-Arctic results across the datasets

Before focusing on the CESM-LE for regional and climate change analyses, we first compare its pan-Arctic performance with the other models and with observations. The ice area monthly lagged correlation in all datasets (Figure 2, upper row) has an initial decline with increased lag, which then is followed by an increase in correlation at lags ranging from a few months to a year. Similar results were found in an earlier version of CESM [*Blanchard-Wrigglesworth et al.*, 2011] and other global climate models (GCMs) [e.g., *Chevallier and Salas-Mélia*, 2012; *Day et al.*, 2014]. The increased correlation at a later time is associated with memory reemergence, and is further categorized into two limbs [*Blanchard-Wrigglesworth et al.*, 2011]: the "summer limb" where the increased correlation is between spring/summer and fall/early winter (also called melt-to-freeze season memory) (Figure 2, upper row, March, May and July panels); and the "winter limb" where the increased correlation is between fall/early winter and the next spring/summer (also called freeze-to-melt season memory) (Figure 2, upper row, January, September, and November panels). PIOMAS, CFSR, the CESM-LE ensemble members, and satellite data all exhibit similar ice area memory reemergence, but there are quantitative differences between the products, particularly in lagged correlations initialized in the spring, summer and fall months. For example, during spring, the ensemble mean of CESM-LE ice area lagged correlation has a slight shift in the timing of the correlation maximum at re-emergence relative to the other products (Figure 2, top row, May panel): local maximum of the black line occurs at lag 7–8 months, while the other products have a local maximum around lag 5. This timing shift likely results from delayed spring melt in CESM relative to observations (Cheng et al., 2014). Moreover, the result from satellite SIC tends to be at the lower end of the CESM ensemble spread, suggesting that CESM-LE overestimates ice area anomaly persistence to an extent, and similar overestimation is also found in other GCMs [*Day et al.*, 2014]. Overestimation by CESM-LE in pan-Arctic mean SST lagged correlation is also present in some parts of a year and here again, quantitative differences exist between PIOMAS, CFSR, and observed SST, even though both CFSR and PIOMAS assimilate SST observation (Figure 2, middle row). Despite their differences, across all data sets, SST lagged correlation has longer decorrelation time scales than that of ice area, and this SST anomaly persistence provides the mechanism for ice area summer limb memory [*Blanchard-Wrigglesworth et al.,* 2011; *Bushuk et al.,* 2014].

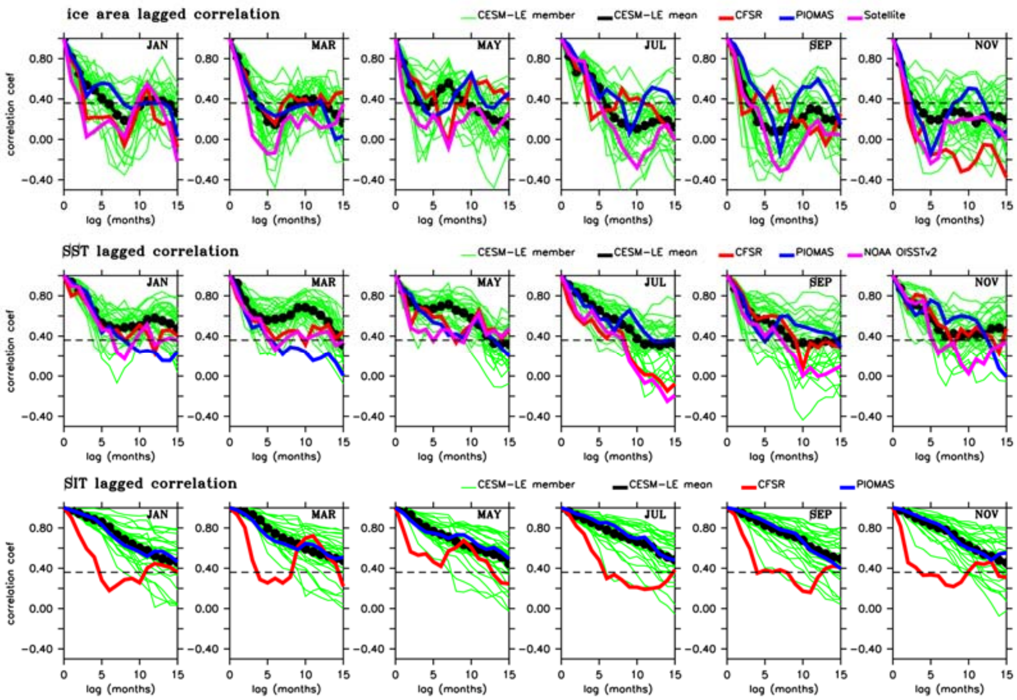

Figure 2. Monthly lagged correlation for pan-Arctic ice area (top row), SST (middle row), and ice thickness anomalies (bottom row) from the CESM-LE 1979-2005 (2005 is the end of CESM historical forcing) (green and black lines), PIOMAS 1979-2014 (blue lines), CFSR 1979-2009 (red lines), and from satellite ice area anomalies using the NASA team algorithm (1979-2014) and NOAA OI SSTv2 (1982-2014) (purple lines). The initial month that is correlated with all other months with lag is marked on the panels. Dashed lines denote the 95% confidence level for statistical significance using one-sided Student's t-test. Note there are no long-term (1979–present) ice thickness satellite data.

Similarly, across-model differences exist in the pan-Arctic mean thickness lagged correlation (Figure 2, bottom row). PIOMAS and the CESM-LE ensemble mean have a similar de-correlation rate through all lags regardless of the initialization month, but the thickness initial de-correlation rate in CFSR is much faster than either CESM-LE or PIOMAS, and the overall shape of ice thickness lagged correlation in CFSR is different from the other two models. Since no long-term ice thickness observation is available for assimilation, modeled ice thickness is subjected to each model's ice physics and parameter values, and the Arctic mean ice thickness monthly climatology differs from one model to another (Figure S1 in supporting material). Difference in model physics, use of data assimilation or lack of it, different air-sea interaction between a coupled model (such as the CESM and CFSR) and an ice-ocean model forced by prescribed atmospheric forcing (such as the PIOMAS), and particularly model physics, affect modeled mean ice thickness and its variability. PIOMAS and CESM-LE have much longer e-folding time scales of Arctic mean ice thickness anomalies than of ice area anomalies: the lagged correlation remains statistically significant (at the 95% confidence level) until lag 20–24 months (not shown). The long decorrelation time scale of the pan-Arctic mean ice thickness provides a mechanism for ice area winter limb memory [*Blanchard-Wrigglesworth et al.*, 2011].

3.2 Pan-Arctic and regional results in the CESM-LE in current climate

Because the lagged correlation patterns of pan-Arctic ice area and thickness anomalies are consistent between the CESM-LE and PIOMAS but only CESM-LE provides a large ensemble and future scenarios, we focus on CESM-LE for regional predictability estimates. For ice area, US Arctic regional results have similar characteristics to pan-Arctic results (Figure 3, upper row). This may not seem surprising, as one expects that pan-Arctic ice area anomalies stem primarily from those along the ice edge or in the regional seas (while the central Arctic basin is fully ice covered with little change). Despite this, each region is influenced by air-sea interaction, ocean circulation, and seasonal migration of the sea ice edge particular to that region, at times causing the regional character to be significantly different from the pan-Arctic mean. For example, during the ice advance season (January to March/April), both the Beaufort and Chukchi seas have significantly lower ice area anomaly persistence than the pan-Arctic area anomalies (Figure 3, upper row, left two panels). This suggests that the latter's persistence originates from other regions of the Arctic. In March, multi-year mean (averaged over 1979-2005) Bering Sea ice area anomalies vary between 30-90% of the Arctic ice area anomalies among the CESM ensemble members; whereas the Chukchi and Beaufort Seas contribute between 1-8% of the Arctic ice area anomalies among the ensemble members. In comparison, during sea ice retreat (Figure 3, upper row, May–September panels), lagged area correlation in the US Arctic regional seas are comparable to that of the pan-Arctic average, suggesting that these seas contribute significantly to the pan-Arctic average. This again is consistent with that in September, multi-year mean ice area anomalies in the Chukchi and Beaufort Seas are 10-50% of the Arctic ice area anomalies, varying among the CESM ensemble members.

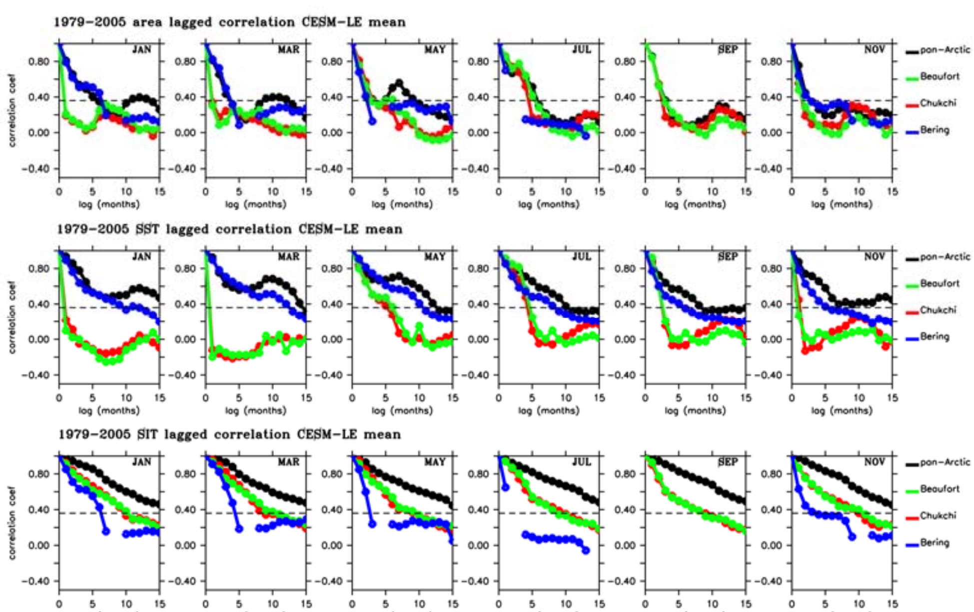

Figure 3. Monthly lagged correlation of ice area (top row), SST (middle row), and ice thickness anomalies (bottom row) in CESM-LE ensemble mean over different regions: pan-Arctic (black lines), Bering Sea (blue lines), Chukchi Sea (red lines), and Beaufort Sea (green lines). The

initial month that is correlated with all other months with lag is marked on the panels. Dashed lines denote the 95% confidence level for statistical significance using one-sided Student's t-test. We used all non-zero data in this calculation without excluding near-constant ice cover months (for example, January–April of the Beaufort Sea).

Regional SST lagged correlation shows considerable spatial and temporal variation. Regions under substantial ice cover and thus insulated from atmospheric forcing have relatively constant SST close to the freezing point, small SST variations (~0.01deg order of magnitude) in these regions and time can be considered as random noise (Figure 3, middle row, January and March panels, Chukchi and Beaufort curve). Aside from these regions and time, regional SST anomalies have significant correlation with lags up to 15 months and later, and the pan-Arctic and Bering Sea SSTs show reemergence associated with winter mixed layer deepening, a mechanism that has also been documented in the observations [e.g., *Alexander et al.*, 1999]. The Bering Sea SST anomaly has weaker lagged correlation than the pan-Arctic mean SST in late fall to early winter, but is comparable to the pan-Arctic mean state in spring and summer (Figure 3, middle row, comparing the black and blue lines). Ice thickness anomalies averaged over the US Arctic regional seas have weaker persistence and a shorter e-folding time scale than the pan-Arctic mean (Figure 3, bottom row). Negative thermodynamic feedback between ice growth and ice thickness causes thinner sea ice to vary more on shorter time scales [e.g., *Bitz and Roe,* 2004]. Such feedbacks, in addition to advective processes, diminish ice thickness anomaly persistence in these regions [*Blanchard-Wrigglesworth and Bitz*, 2014]. By this metric, the Beaufort and Chukchi seas have similar ice thickness e-folding time scales, and both are longer than that of the Bering Sea. This is likely because the Bering Sea on average has thinner sea ice than the other two regions.

3.3 Influence of changing climate

As mentioned before, the pan-Arctic ice area anomaly possesses two types of memory re-emergence: one is the melt-to-freeze season/summer limb memory associated with SST anomalies created at the retreating ice edge and its persistence, and the other is the freeze-to-melt season/winter limb memory enabled by long e-folding time scales of ice thickness variations (Figure 3). Figure 4 illustrates both types of memory in the CESM-LE, for the pan-Arctic mean (left column) and Chukchi Sea ice area anomalies (right column). Lagged correlation of ice area anomalies is calculated for each sequential 35-year period beginning in 1920 and ending in 2080 (e.g., 1920-1954, 1921-1955, … 2046-2080) across the CESM-LE ensemble members. Results suggest that the summer limb memory of the pan-Arctic ice area anomalies is stronger and occurs later in a warmer climate (area denoted by red dashed lines in Figure 4a, left columns; and Figure 4b, left column, comparing areas centered around lag 3-4 months across the panels) – the elevated correlation with July ice area anomalies occurs in September, October, and November, respectively, in the 1920–1954, 2006–2040, and 2041–2075 climates. As the climate warms, mean Arctic Ocean stratification increases (Figure S2 in supporting material), along with increases in open water area and duration. These changes lead to more persistent upper ocean property anomalies in warmer climate, which contribute to stronger ice area summer limb memory because the summer limb memory depends on SST and upper ocean property changes. In addition, because of the stronger future decline in autumn SIC relative to early summer SIC, a robust feature of Arctic amplification seen in CESM and other GCMs, the present-day co-location of July and October SIC anomalies that is crucial for the timing of summer limb memory reemergence [*Blanchard-Wrigglesworth et al.*, 2011] evolves into a future July–

November co-location of SIC anomalies (supporting material, Figure S3). However, there are across-region variations in sea ice predictability change with changing climate. For example, ice area anomalies in the Chukchi Sea have similar delayed summer-to-fall reemergence as the pan-Arctic mean state but slight weakening in the lagged correlation coefficients in the second half of 21st century relative to earlier time based on the ensemble mean result (Figure 4a, right column), but large variations exist across the ensemble members (Figure 4b, right column). Beaufort Sea ensemble mean result shows a similar delay of summer ice area memory reemergence in the future as in the pan-Arctic mean state and Chukchi Sea, but there is less weakening of the correlation coefficients with time compared to the Chukchi Sea (Figure S4, in supporting material). Concurrently, the winter limb of pan-Arctic ice area memory weakens as climate warms (Figure 4a, areas denoted by blue dashed lines; and Figure 4b, comparing areas centered around lag 13-14 months across the panels), likely due to thinning of Arctic mean ice thickness (supporting material, Figure S1), but again, across-region variations and large inter-member variation across the ensemble persist (Figure 4, Figure S4 in supporting material). Ice area winter limb memory is associated with ice thickness anomaly persistence, and ice thickness variability is strongly heterogeneous in space, hence the across-region differences in winter limb memory change. These results stress spatial heterogeneity in Arctic sea ice changes with changing climate. For the pan-Arctic mean state, the effect of warming on summer limb memory is obvious by the first half of 21st century (e.g., 2006–2040), whereas warming doesn't appear to significantly alter the winter limb memory until the second half of 21st century (e.g., 2041-2075).

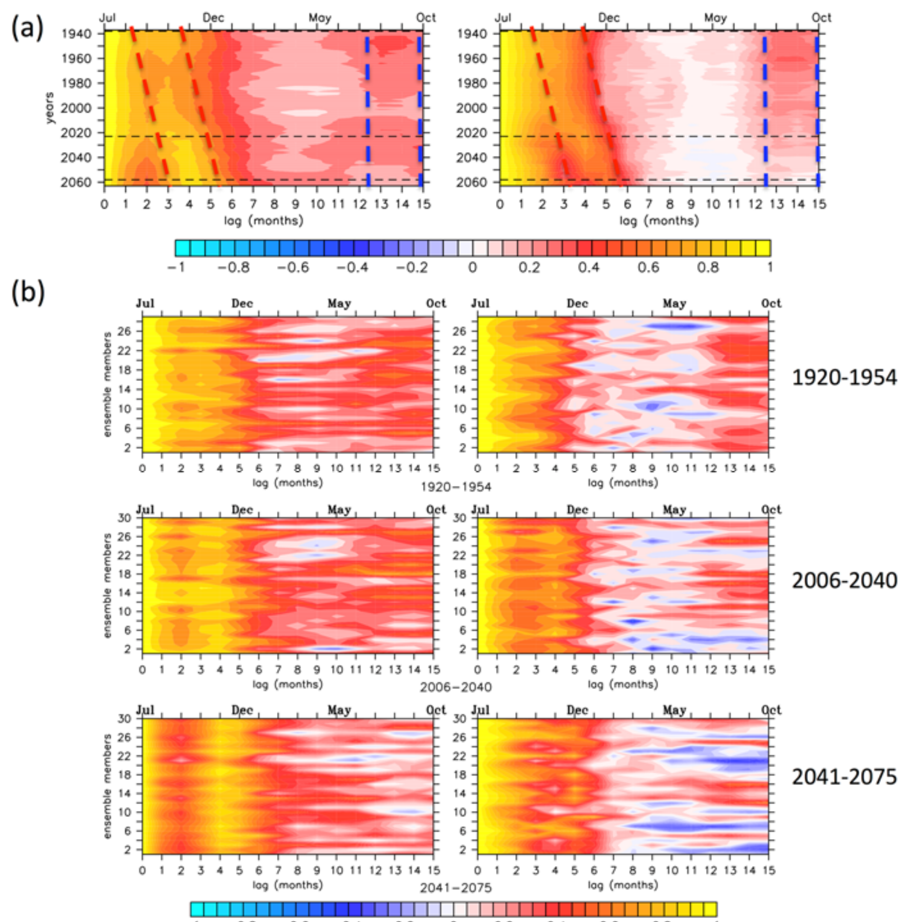

Figure 4. (a) Monthly lagged correlation of pan-Arctic (left column) and Chukchi Sea (right column) ice area anomalies, from the CESM-LE ensemble mean. Calculation is done for all sequential 35-year periods beginning in 1920 and ending in 2080, and the y-axis corresponds to the center of each of the 35-year periods. X-axis is lag in months, with lag-0 corresponding to July. Months corresponding to lag-0, lag-5, lag-10, and lag-15 are marked on the top of each panel. Horizontal dashed lines correspond to the middle year of the three time periods shown in (b). (b) As in (a) but showing the ensemble spread of CESM-LE for three periods: 1920–1954 (top row), representing the 20th century mean climate before significant warming; 2006–2040 (middle row) and 2041–2075 (bottom row), representing the 21st century warmed climates with varying degrees. The red dashed lines in a) highlight the summer limb memory change and timing delay as climate warms, while the blue dashed lines highlight concurrent changes in the ice area memory from one summer to the next.

4 Discussion and Conclusions

We investigate an aspect of sea ice predictability over the pan-Arctic domain and in the US Arctic regional seas using lagged correlation, a diagnostic predictability metric. We analyzed output from the CESM-LE, PIOMAS, and CFSR models and satellite microwave SIC and SST observations. These models are either coupled earth system models (one with data assimilation and one without) or stand-alone ice-ocean model assimilating ocean and atmosphere observation. We identify common as well as diverging model behavior to better understand inherent sea ice predictability limits. All three models' output, as well as the satellite SIC, exhibits pan-Arctic ice area memory reemergence even though the exact magnitudes of lagged correlation differ across the models, as well as between each of the models and satellite observation (Figure 2). Therefore, uncertainties remain in the Arctic sea ice modeling, even with the help of data assimilation. Despite such uncertainties, monthly ice thickness lagged correlation is similar between CESM-LE and PIOMAS, while CFSR has a much shorter ice thickness e-folding time scale than both CESM-LE and PIOMAS for all seasons.

Lagged correlation of ice property and SST in the regional seas vary strongly with location and season (Figure 3). For example, the Beaufort and Chukchi seas have much weaker ice area anomaly persistence during the winter season (January-March/April) than either the Bering Sea or the pan-Arctic mean anomaly (Figure 3, upper row, January and March panels). Although the Beaufort and Chukchi seas are nearly completely ice covered during the winter months, there is some ice area variability in these regions due to opening and closing of coastal polynyas [*Ladd et al.,* 2016], and these wind-driven processes have little memory or persistence from one month to the next.

Compared to pan-Arctic ice area anomalies, the pan-Arctic ice thickness and SST anomalies are much more persistent, but such persistence decreases on regional scales (Figure 3). Ice thickness variability is governed by thermodynamic growth/melt and dynamic transport as well as ridging processes. Regional ice thickness gains or losses that are driven by dynamics (ice of different thickness being advected from one region into another) cancel out for the pan-Arctic average, allowing the latter to have stronger persistence than most sub-regions. Likewise, advection could diminish SST anomaly persistence over a particular region [e.g., *Serreze et al.*, 2016], but has weak effect on pan-Arctic mean SST anomalies. Taken together, these results suggest that predictability of ice area in the US Arctic regional seas is generally weaker than that of the pan-Arctic mean state.

As climate warms, Arctic ice thins and open water duration and coverage increases, the pan-Arctic ice area summer limb memory increases but the winter limb memory decreases; in addition, the summer-to-fall memory reemergence occurs later in warmer climates (Figure 4), consistent with delayed fall freeze-up. However, there are across-region variations in sea ice predictability changes with changing climate. These results invite questions such as: How much warming and thinning is necessary before ice predictability in the Arctic is affected? What regions of the Arctic are most sensitive to climate state changes? With more observational data becoming available and climate and sea ice models continuing to improve, we can begin to address these questions.

Acknowledgments and Data

This material is based on work supported by NOAA/OAR under the auspices of the National Earth System Prediction Capability (National ESPC) and ONR N000141310793. This is NOAA/PMEL publication number 4540. This publication is partially funded by the Joint Institute for the Study of the Atmosphere and Ocean (JISAO) under NOAA Cooperative Agreement NA10OAR4320148 (2010-2015) and NA15OAR4320063 (2015-2020). This research is contribution EcoFOCI-0875 to NOAA's Ecosystems and Fisheries-Oceanography Coordinated Investigations. Model outputs and satellite data used in this study are all referenced and publicly accessible. The lagged correlation results are available from the authors upon request (wei.cheng@noaa.gov). We thank the modeling groups for making their data available for analysis. We also thank Dr. Marika Holland for helpful discussions, and Dr. Mitch Bushuk and two anonymous reviewers for their constructive comments on an earlier version of the manuscript.

References

Alexander, M.A., C. Deser, and M.S. Timlin (1999), The reemergence of SST anomalies in the North Pacific Ocean. *J. clim.*, *12*(8), 2419-2433.

Bitz, C. M., and G. H. Roe (2004), A mechanism for the high rate of sea ice thinning in the Arctic Ocean, *J. Clim.*, *17*(18), 3623–3632.

Blanchard-Wrigglesworth, E., and C. M. Bitz (2014), Characteristics of Arctic sea ice thickness variability in GCMs, *J. Clim.*, *27*(21), 8244–8258.

Blanchard-Wrigglesworth, E., K. C. Armour, C. M. Bitz, and E. DeWeaver (2011), Persistence and inherent predictability of Arctic sea ice in a GCM ensemble and observations, *J. Clim.*, *24*(1), 231–250.

Brown, Z. W., and K. R. Arrigo (2013), Sea ice impacts on spring bloom dynamics and net primary production in the Eastern Bering Sea, *J. Geophys. Res. Oceans*, *118*(1), 43–62.

Bushuk, M., D. Giannakis, and A. J. Majda (2014), Reemergence mechanisms for North Pacific sea ice revealed through nonlinear Laplacian spectral analysis, *J. Clim.*, 27, 6265–6287.

Cavalieri, D. J., and C. L. Parkinson (2012), Arctic sea ice variability and trends, 1979–2010, *The Cryosphere*, *6*, 881–889.

Chevallier, M., and D. Salas-Mélia (2012), The role of sea ice thickness distribution in the Arctic sea ice potential predictability: A diagnostic approach with a coupled GCM. *J. Clim.*, 25, 3025-3038.

Comiso, J. C., and D. K. Hall (2014), Climate trends in the Arctic as observed from space, *WIREs Clim Change, 5*, 389-409, doi: 10.1002/wcc.277.

Cheng, W., E. Curchitser, C. Ladd, P. Stabeno, and M. Wang (2014), Influences of sea ice on the Eastern Bering Sea: NCAR CESM simulations and comparison with observations, *Deep Sea Res. Part II Top. Stud. Oceanogr.*, *109*, 27–38.

Day, J. J., S. Tietsche, and E. Hawkins (2014), Pan-Arctic and regional sea ice predictability: initialization month dependence, *J. Clim.*, *27*(12), 4371–4390.

Holland, M. M., D. A. Bailey, and S. Vavrus (2011), Inherent sea ice predictability in the rapidly changing Arctic environment of the Community Climate System Model, version 3, *Clim. Dyn.*, *36*(7), 1239–1253.

Kay, J. E., et al. (2015), The Community Earth System Model (CESM) Large Ensemble Project: A community resource for studying climate change in the presence of internal climate variability, *Bull. Am. Meteorol. Soc.*, *96*(8), 1333–1349.

Ladd, C., C. W. Mordy, S. A. Salo, and P. J. Stabeno (2016), Winter water properties and the Chukchi Polynya, *J. Geophys. Res. Oceans*, doi:10.1002/2016JC011918, in press.

Lindsay, R. W., and J. Zhang (2006), Assimilation of ice concentration in an ice–ocean model, *J. Atmospheric Ocean. Technol.*, *23*(5), 742–749.

Massonnet, F., T. Fichefet, H. Goosse, C. M. Bitz, G. Philippon-Berthier, M. M. Holland, and P.-Y. Barriat (2012), Constraining projections of summer Arctic sea ice, *The Cryosphere, 6*, 1383–1394.

Meier, W., F. Fetterer, M. Savoie, S. Mallory, R. Duerr, and J. Stroeve (2013, updated 2015), *NOAA/NSIDC Climate Data Record of Passive Microwave Sea Ice Concentration, Version 2*. Boulder, Colorado USA. NSIDC: National Snow and Ice Data Center. doi:10.7265/N55M63M1. Accessed July 07, 2016.

Peng, G., W. Meier, D. Scott, and M. Savoie (2013), A long-term and reproducible passive microwave sea ice concentration data record for climate studies and monitoring, *Earth Syst. Sci. Data*, 5, 311–318.

Reynolds, R. W., T. M. Smith, C. Liu, D. B. Chelton, K. S. Casey, and M. G. Schlax (2007), Daily high-resolution-blended analyses for sea surface temperature, *J. Clim.*, 20, 5473–5496.

Saha, S., et al. (2010), The NCEP Climate Forecast System Reanalysis, *Bull. Am. Meteorol. Soc.*, *91*(8), 1015–1057.

Schweiger, A., R. Lindsay, J. Zhang, M. Steele, H. Stern, and R. Kwok (2011), Uncertainty in modeled Arctic sea ice volume, *J. Geophys. Res. Oceans*, *116*(C8), C00D06, doi:10.1029/2011JC007084.

Serreze, M. C., A. D. Crawford, J. C. Stroeve, A. P. Barrett, and R. A. Woodgate (2016), Variability, trends, and predictability of seasonal sea ice retreat and advance in the Chukchi Sea. *J. Geophys. Res. Oceans*, 121, doi:10.1002/2016JC011977.

Stabeno, P. J., N. B. Kachel, S. E. Moore, J. M. Napp, M. Sigler, A. Yamaguchi, and A. N. Zerbini (2012), Comparison of warm and cold years on the southeastern Bering Sea shelf and some implications for the ecosystem, *Deep-Sea Res. II*, 65–70, 31–45.

Tietsche, S., J. J. Day, V. Guemas, W. J. Hurlin, S. P. E. Keeley, D. Matei, R. Msadek, M. Collins, and E. Hawkins (2014), Seasonal to interannual Arctic sea ice predictability in current global climate models, *Geophys. Res. Lett.*, *41*(3), 1035–1043.

Wang, W., M. Chen, and A. Kumar (2012), Seasonal prediction of Arctic sea ice extent from a coupled dynamical forecast system, *Mon. Weather Rev.*, *141*(4), 1375–1394.

Woodgate, R. A., K. Aagaard, and T. J. Weingartner (2005), Monthly temperature, salinity, and transport variability of the Bering Strait through flow, *Geophys. Res. Lett.*, *32*(4), L04601, doi:10.1029/2004GL021880.

Wyllie-Echeverria, T., and W. S. Wooster (1998), Year-to-year variations in Bering Sea ice cover and some consequences for fish distributions, *Fish. Oceanogr.*, 7, 159–170.

Zhang, J., and D. A. Rothrock (2003), Modeling global sea ice with a thickness and enthalpy distribution model in generalized curvilinear coordinates, *Mon. Weather Rev.*, *131*(5), 845–861.

Geophysical Research Letter

Supporting Information for

Diagnostic sea ice predictability in the pan-Arctic and US Arctic regional seas

Wei Cheng[1,2], Edward Blanchard-Wrigglesworth[3], Cecilia M. Bitz[3], Carol Ladd[2], and Phyllis J. Stabeno[2]

[1]University of Washington, Joint Institute for the Study of Atmosphere and Ocean, Seattle, Washington, USA.

[2]NOAA/Pacific Marine Environmental Laboratory, Seattle, Washington, USA.

[3]University of Washington, Department of Atmospheric Science, Seattle, Washington, USA.

Corresponding author: Wei Cheng (wei.cheng@noaa.gov)

Contents of this file

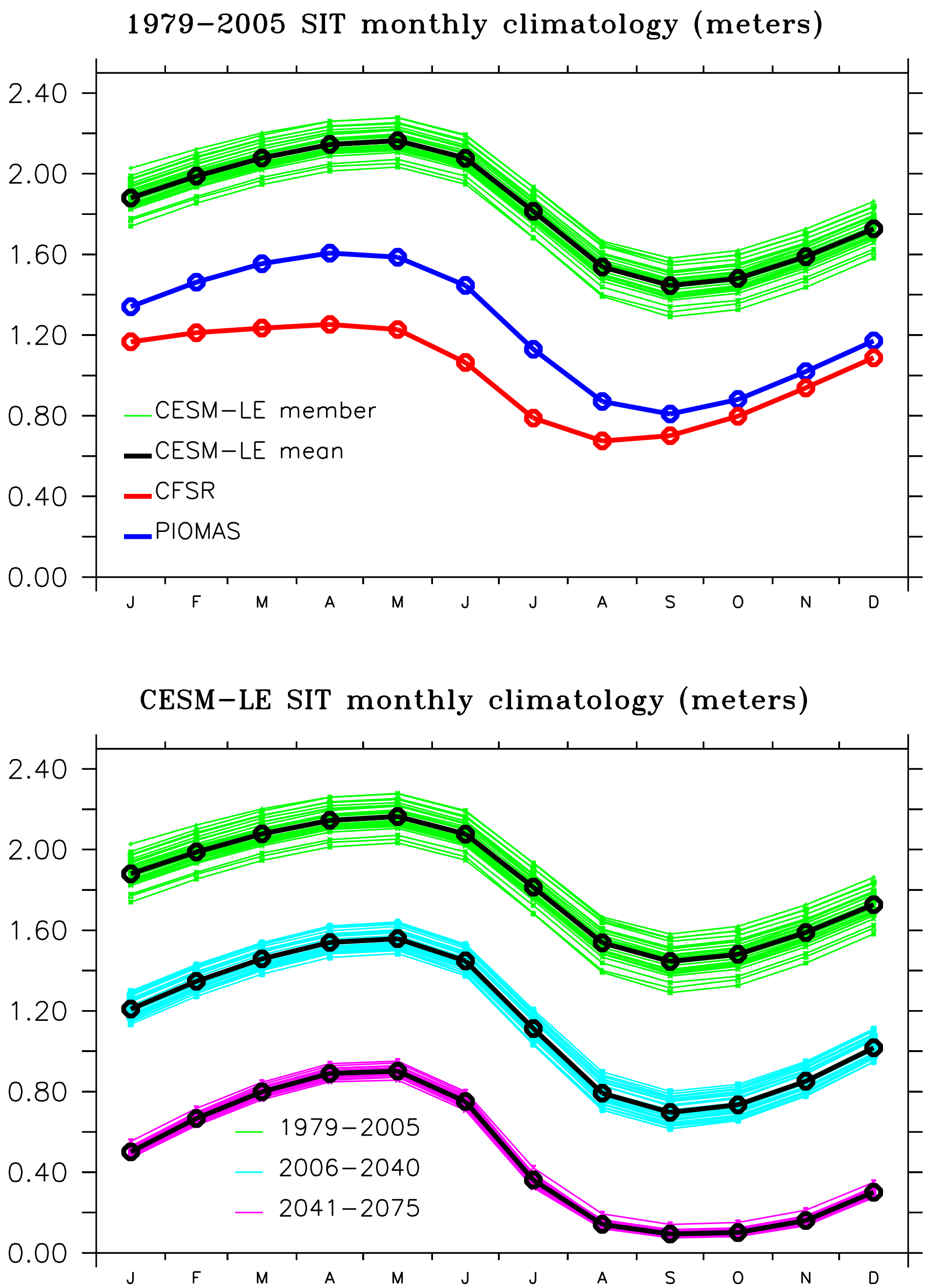

Figure S1. Mean Arctic (north of 55°N) ice thickness monthly climatology based on years 1979-2005, from CESM-LE, CFSR, and PIOMAS (top), and from CESM-LE over different time periods (bottom).

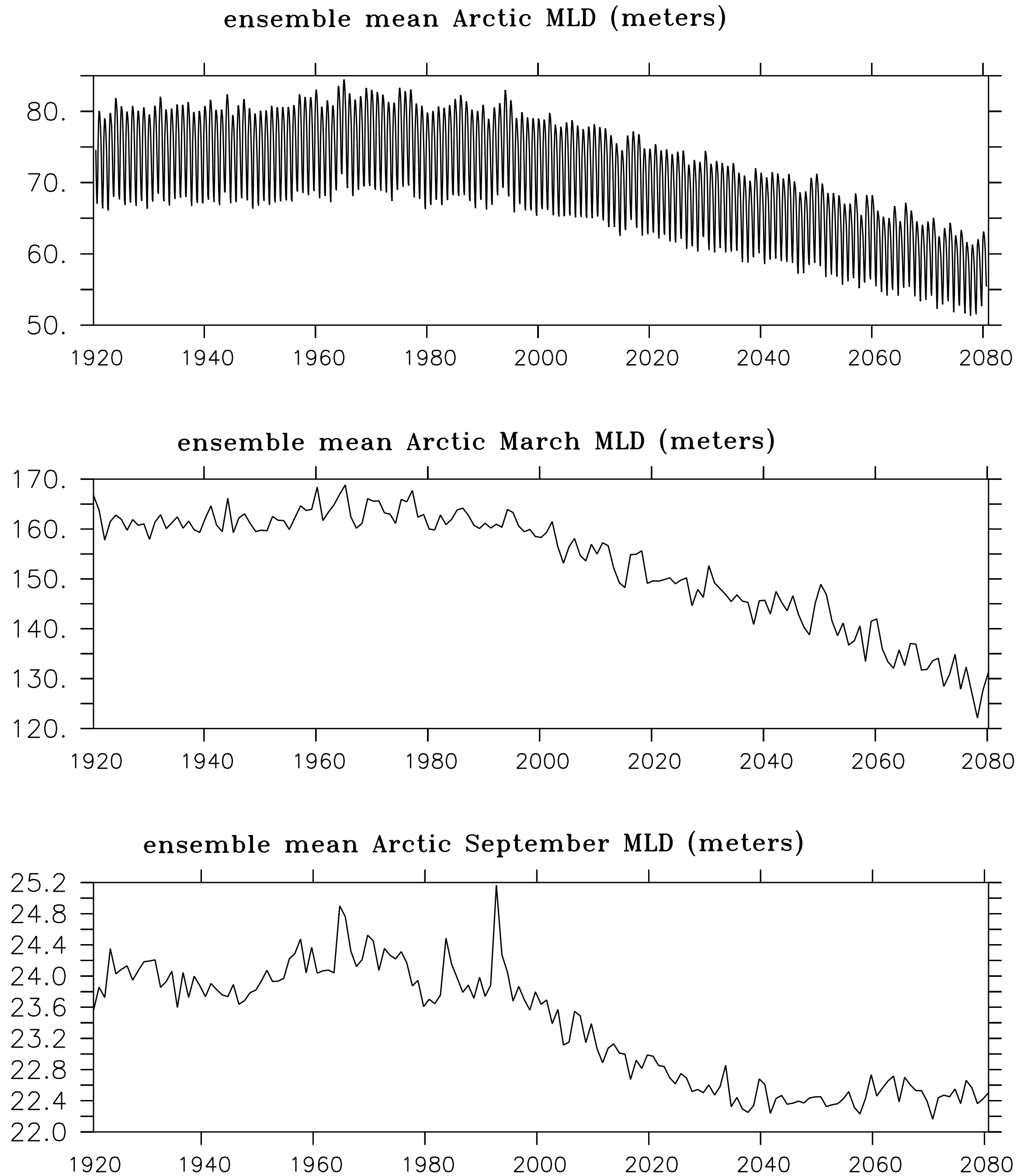

Figure S2. Time series of mixed layer depth (MLD) in the Arctic (averaged north of 55°N) from CESM-LE ensemble mean, showing monthly MLD smoothed by a 11-point running box (top), March (middle) and September (bottom) of each year. Decrease of MLD with time suggests increase in the Arctic upper ocean stratification.

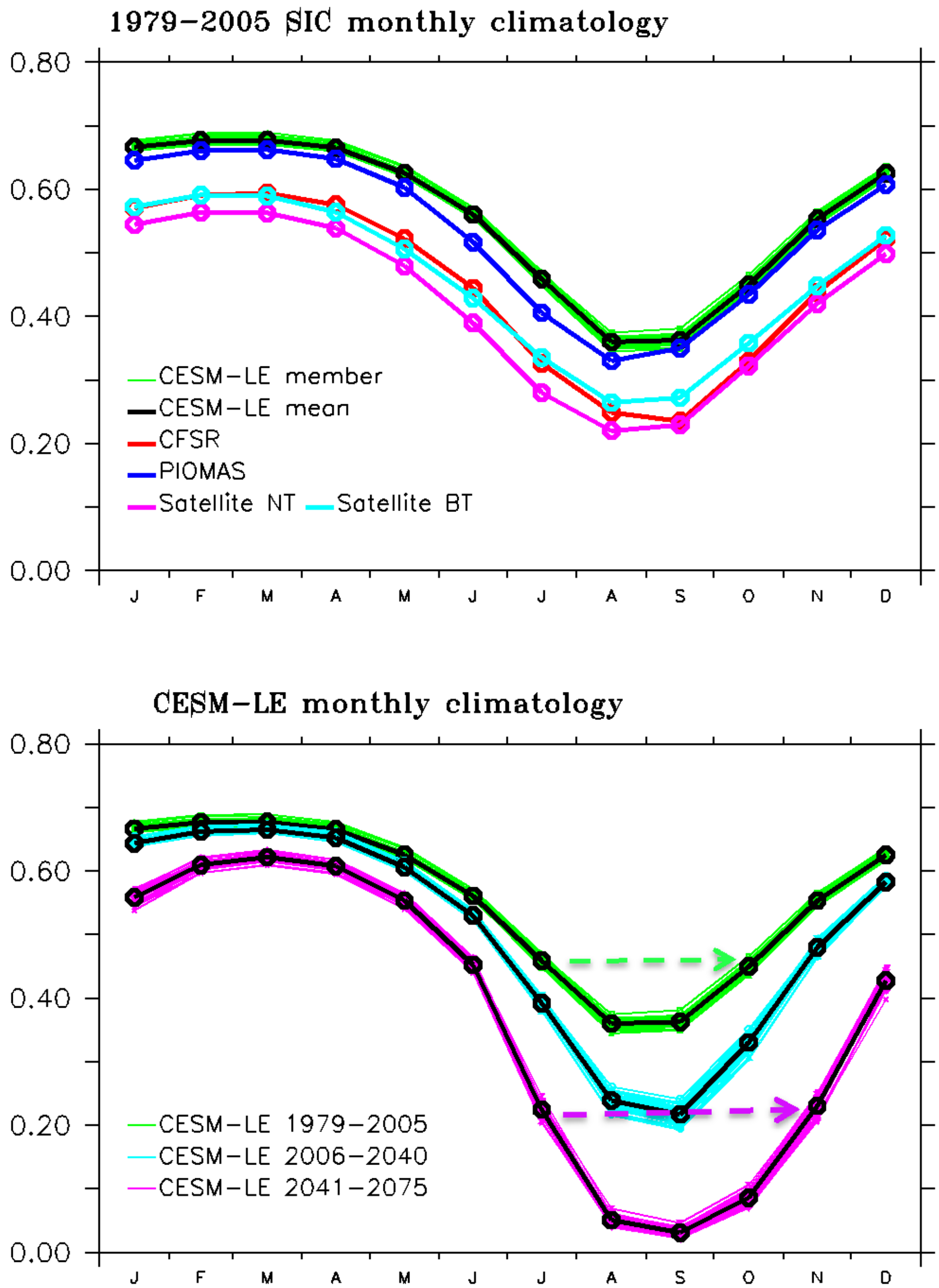

Figure S3. Mean Arctic (north of 55°N) sea ice concentration (SIC) monthly climatology based on years 1979-2005, from CESM-LE, CFSR, PIOMAS, and satellite data (showing both the NASA team and boot strap algorithms) (top) and from CESM-LE over different time periods (bottom). Dashed arrows in the bottom panel highlight the months with similar SIC values (therefore these months have similarly located ice edge), and how such seasonality changes from present-day July-to-October co-location to future July-to-November co-location.

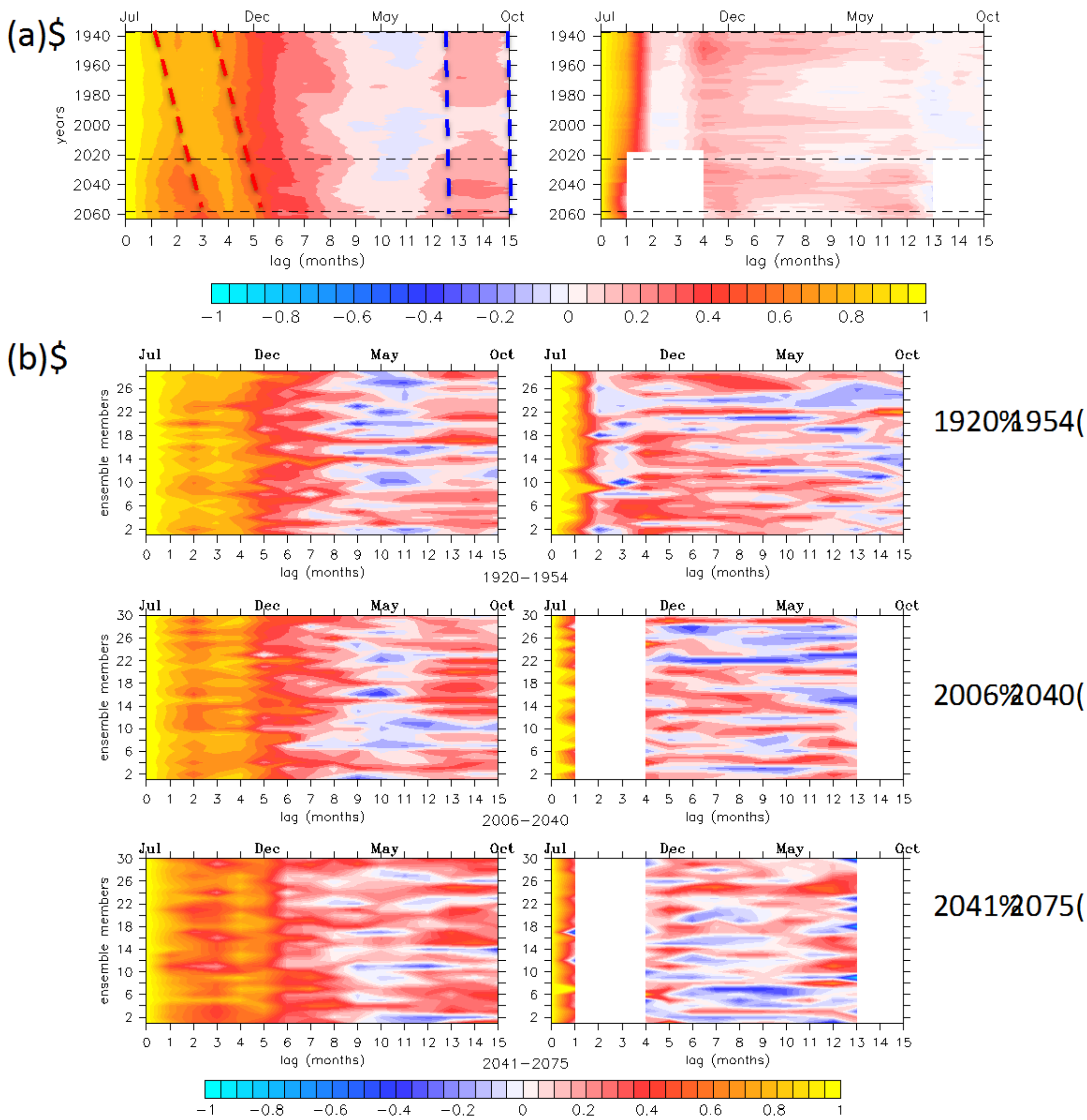

Figure S4. As in Figure S4 but for the Beaufort Sea (left columns) and Bering Sea (right columns). White areas in the right columns indicate that the Bering Sea is ice-free in those months.